



Precipitation oxygen isotope variability across timescales in East Asia records two sub-processes of summer monsoon system



Zhaowei Jing^{1,2}, Zhengyu Liu^{3,4}✉, Shaoqing Zhang^{1,5}✉, Qin Wen^{6,7,8}, Chengfei He⁹, Yuntao Bao³ & Wusheng Yu¹⁰

The seasonal variation of precipitation isotopes ($\delta^{18}\text{O}_p$) exhibits a north-south dipole in the East Asian monsoon region, correlating with temperature in northern China and precipitation in southern China. However, on longer timescales, $\delta^{18}\text{O}_p$ tends to exhibit spatial coherence. This inconsistency in $\delta^{18}\text{O}_p$ variability across different timescales has sparked considerable debate regarding their climatic interpretation. Here we develop a unified framework to quantify the mechanisms driving $\delta^{18}\text{O}_p$ variability across timescales using water tagging experiments in iCAM5.3 numerical model. Our results demonstrate that $\delta^{18}\text{O}_p$ variations are governed primarily by monsoon-driven changes in moisture source and enroute depletion, rather than local meteorological factors. Furthermore, the relative importance of these processes differs across timescales. Therefore, the evolution of the East Asian summer monsoon, as recorded in $\delta^{18}\text{O}_p$, should be interpreted through the lens of these two sub-processes of the monsoon system, rather than based solely on the empirical isotopic effects observed on seasonal timescales.

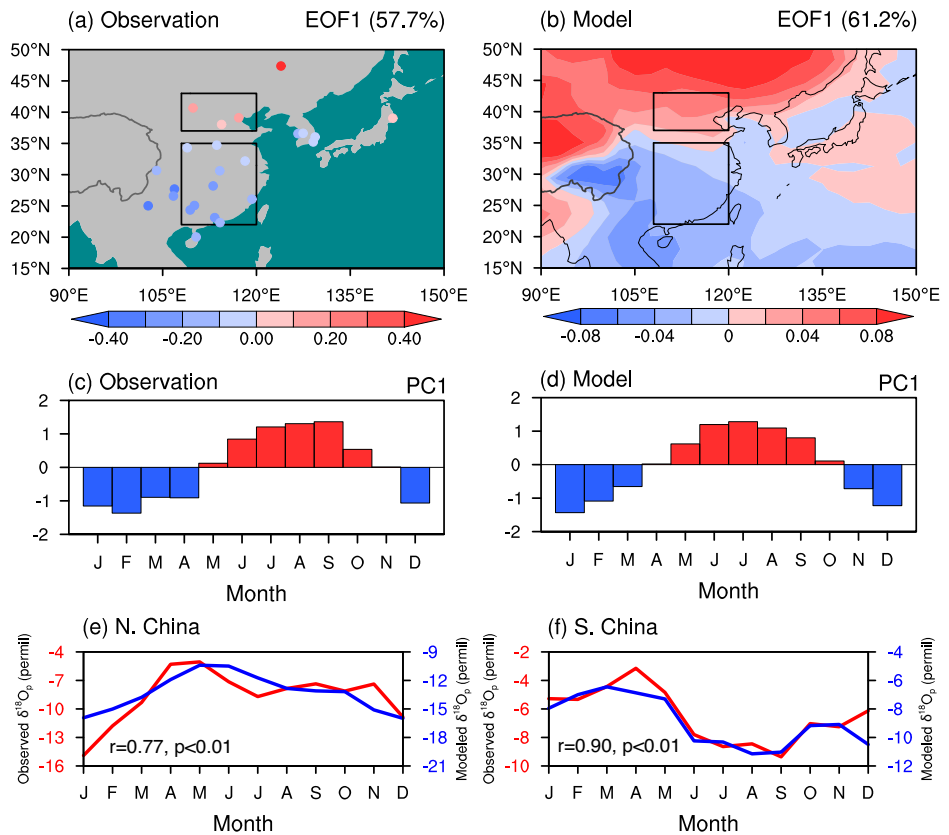
The spatiotemporal variation of stable water isotope ratios in modern precipitation ($\delta^{18}\text{O}_p$) shows clear patterns that strongly correlate with several environmental variables^{1,2}. Dansgaard¹ was the first to analyze $\delta^{18}\text{O}_p$ data comprehensively, identifying empirical relationships between $\delta^{18}\text{O}_p$ variations with several environmental factors across space, notably surface temperature and precipitation amount. Two well-known effects were observed: the “temperature effect”, where $\delta^{18}\text{O}_p$ becomes more enriched with higher temperatures, and the “amount effect”, where $\delta^{18}\text{O}_p$ is depleted with increased precipitation^{1–3}. Both effects are thought to be influenced by the Rayleigh distillation. These effects have also been used to infer climatic changes over various timescales, from seasonal to orbital cycles^{4–7}. However, climatic interpretations of $\delta^{18}\text{O}_p$ across different timescales are often studied separately without a unified framework, leaving it a great challenge to connect

long-term climate changes from paleoclimate records with present short-term observations, especially in the East Asian Monsoon (EAM) region.

Present observations reveal contrasting seasonal $\delta^{18}\text{O}_p$ patterns in northern and southern China. In northern China, the “temperature effect” dominates, while in southern China, the “amount effect” is more prominent^{4,8–10}. However, these seasonal relationships are insufficient to explain longer-term climate changes. In proxy records and climate model simulations, $\delta^{18}\text{O}_p$ shows variability from interannual to millennial and orbital timescales, which can sometimes decouple from local temperature in northern China^{11,12} or local precipitation amount in southern China^{9,13,14}. Furthermore, $\delta^{18}\text{O}_p$ exhibits coherent changes across the entire EAM region on interannual^{15–17}, millennial^{18–20}, and orbital timescales^{21–23}, despite the differing seasonal cycles between southern and northern China (Fig. 1a, b).

¹School of Ecology and Nature Conservation, Beijing Forestry University, Beijing, China. ²Laoshan Laboratory, Qingdao, China. ³Department of Geography, The Ohio State University, Columbus, OH, USA. ⁴School of Geography Science, Nanjing Normal University, Nanjing, China. ⁵International Laboratory for High-Resolution Earth System Model and Prediction (iHESP), Qingdao, China. ⁶School of Geography, Nanjing Normal University, Nanjing, China. ⁷Key Laboratory of Virtual Geographic Environment (Nanjing Normal University), Ministry of Education, Nanjing, China. ⁸Jiangsu Center for Collaborative Innovation in Geographical Information Resource Development and Application, Nanjing, China. ⁹Department of Marine & Environmental Sciences, Northeastern University, Nahant, USA. ¹⁰State Key Laboratory of Tibetan Plateau Earth System, Environment and Resources (TPESER), Institute of Tibetan Plateau Research, Chinese Academy of Sciences, Beijing, China. ✉e-mail: liu.7022@osu.edu; szhang@ouc.edu.cn

Fig. 1 | EOF analysis of the seasonal cycle of $\delta^{18}\text{O}_p$ over the EAM region and its surroundings. a The leading EOF mode (EOF1) of observed $\delta^{18}\text{O}_p$. **b** The EOF1 of modeled $\delta^{18}\text{O}_p$. **c** The leading principal components (PC1) of observed $\delta^{18}\text{O}_p$. **d** The PC1 of modeled $\delta^{18}\text{O}_p$. **e** Seasonal cycle of observed (red) and simulated (blue) $\delta^{18}\text{O}_p$ in northern China (N. China). **f** Seasonal cycle of observed (red) and simulated (blue) $\delta^{18}\text{O}_p$ in southern China (S. China). The percentage values in the top right of (a, b) represent the variance explained by EOF1. In (a, b), the upper and bottom black boxes mark the regions of N. China (37°N to 43°N, 108°E to 120°E) and S. China (22°N to 35°N, 108°E to 120°E), respectively. The dark gray lines outline the part of the Tibetan Plateau boundary. Detailed information regarding the observed $\delta^{18}\text{O}_p$ is provided in Supplementary Table 1. The modeled $\delta^{18}\text{O}_p$ is derived from the final 20 years of a 40-year PI water tagging experiment.



The complexity of interpreting $\delta^{18}\text{O}_p$ across different timescales is partly due to the influence of remote moisture sources and transport patterns, which can exert a much greater influence on $\delta^{18}\text{O}_p$ than local temperature or precipitation alone²⁴. In the EAM region, the seasonal variation in moisture sources and the meridional shift of moisture transport patterns, both driven by the monsoon system, significantly complicate the climatic interpretation of $\delta^{18}\text{O}_p$. As a result, several other factors, such as changes in precipitation and moisture sources^{4,15,25–31}, enroute depletion and upstream rainout/convection^{12,13,17,32–43}, monsoon intensity^{44,45}, and precipitation seasonality^{23,35,46–50}, have been proposed to explain $\delta^{18}\text{O}_p$ variations. However, these factors are often interrelated, making it challenging to isolate them. For example, changes in summer monsoon moisture sources are often coincide with enhanced upstream convection. Despite the EAM's influence on both northern and southern China, it remains unclear how these monsoon-related factors contribute to the contrasting seasonal $\delta^{18}\text{O}_p$ cycles in the two regions while also explaining the coherent $\delta^{18}\text{O}_p$ changes on longer timescales.

To address these issues, we quantitatively analyze $\delta^{18}\text{O}_p$ variations in northern and southern China across seasonal, millennial, and orbital timescales using a unified framework in a state-of-the-art isotope-enabled earth system model. This unified framework reveals that the main distinction between the $\delta^{18}\text{O}_p$ variations in seasonal and longer timescale lies in the additional impact of precipitation seasonality in the latter. Otherwise, both are controlled by the same processes in the water cycle, including changes in moisture sources and a series of source-to-enroute-to-condensation processes. Our results show that change in moisture sources and upstream enroute depletion are the two primary factors controlling $\delta^{18}\text{O}_p$ variability in the EAM region, with their importance varying across different timescales. Change in moisture source dominate $\delta^{18}\text{O}_p$ variability on seasonal and orbital timescales, while meltwater-induced enroute depletion is the main driver on millennial timescales. The contrasting seasonal cycles of the $\delta^{18}\text{O}_p$ between northern and southern China are mainly due to seasonal changes in moisture source from remote regions, where the contributed $\delta^{18}\text{O}_p$ values

are very depleted, with minimal contribution from local change of temperature or precipitation amount.

Results and discussion

Model-data comparison

Our pre-industrial (PI) simulation in iCAM5.3 reproduces the major feature of the observed seasonal $\delta^{18}\text{O}_p$ cycle in the EAM region. It shows a clear contrast between the “temperature effect” in northern China and the “amount effect” in southern China, as shown by the leading EOFs (Fig. 1; Supplementary Fig. 1; see Methods, Part 1). Additionally, our model accurately reproduces the spatial pattern of seasonal $\delta^{18}\text{O}_p$ variations in the EAM region. Specifically, both the observation and simulation show that the $\delta^{18}\text{O}_p$ enrichment in summer gradually become more pronounced with latitude in the northern part of the EAM region, while $\delta^{18}\text{O}_p$ depletion in summer is most pronounced in southwestern China (Fig. 1a, b). The direct model-data comparison shows good agreement between the simulated and observed $\delta^{18}\text{O}_p$ in North China ($r = 0.77$, $p < 0.01$) and South China ($r = 0.90$, $p < 0.01$) (Fig. 1e, f).

Moisture source ($\Delta_{\text{dP}_{\text{on}}}$) dominates the seasonal $\delta^{18}\text{O}_p$ anomaly over the EAM region

The seasonal variation of $\delta^{18}\text{O}_p$ (anomaly from the annual mean) is influenced by moisture from different source regions (see Methods, Part 2). In northern China, although most precipitation comes from local East Asia continent (EAS) throughout the year (Supplementary Fig. 2a, e), this has little impact on the seasonal cycle of $\delta^{18}\text{O}_p$ (Fig. 2a). In contrast, the remote North Atlantic Ocean (AO), with much more depleted $\delta^{18}\text{O}_p$ (Supplementary Fig. 2c), plays a crucial role in producing the apparent “temperature effect” in northern China (Fig. 2a). To understand how each source region contributes to the seasonal cycle of $\delta^{18}\text{O}_p$, we decompose the $\delta^{18}\text{O}_p$ anomaly into two components: $\Delta\delta^{18}\text{O}_p = \Delta_{\text{dP}_{\text{on}}} + \Delta_{\text{d}\delta}$, where $\Delta_{\text{dP}_{\text{on}}}$ represents the precipitation weight change from the source region and $\Delta_{\text{d}\delta}$ represents the

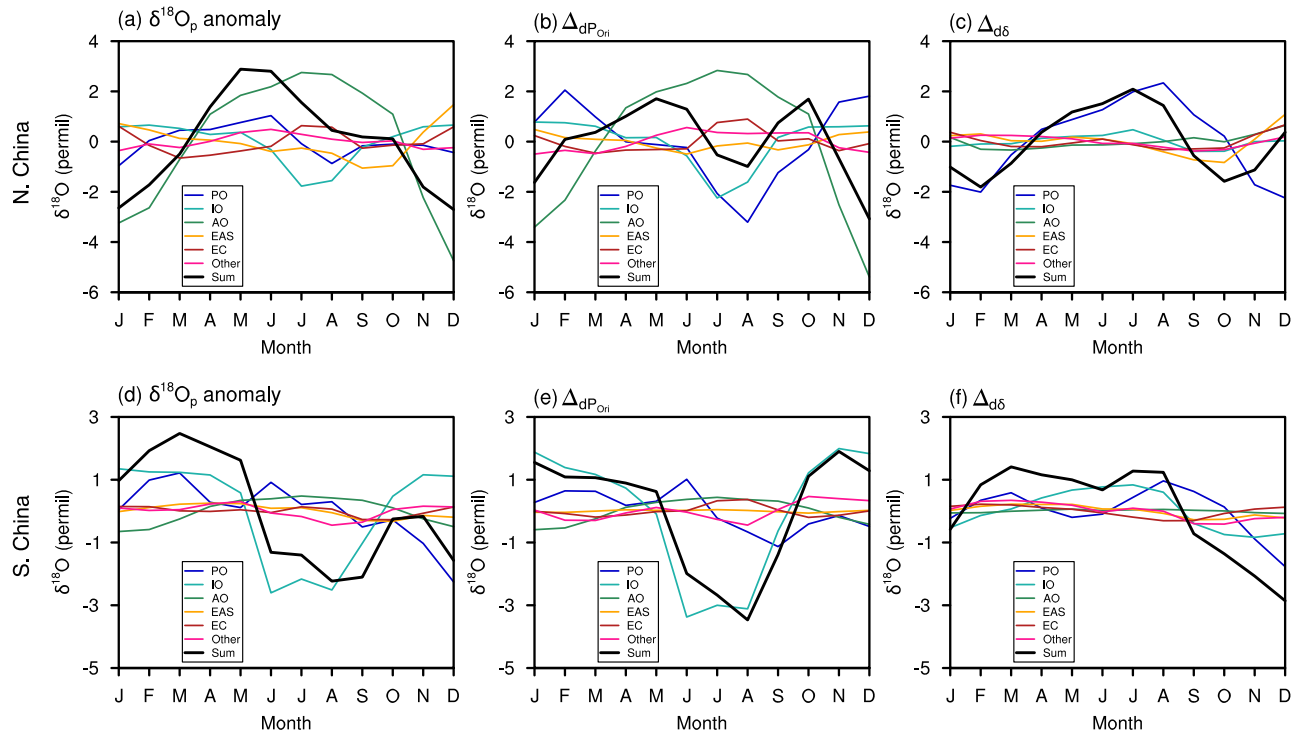


Fig. 2 | Seasonal $\delta^{18}\text{O}_p$ variations and its decomposition in N. China and S. China. **a** Seasonal $\delta^{18}\text{O}_p$ anomaly (bold black line) and its source decomposition (non-black lines) in N. China. **b** Contribution of moisture source change to the $\delta^{18}\text{O}_p$ anomaly ($\Delta_{dP_{Ont}}$, bold black line) and the source decomposition of $\Delta_{dP_{Ont}}$ (non-black lines) in N. China. **c** Contribution of isotope change from source regions to the $\delta^{18}\text{O}_p$ anomaly ($\Delta_{d\delta}$, bold black line) and the source decomposition of $\Delta_{d\delta}$ (non-black

lines) in N. China. **d** Same as (a) but for S. China. **e** Same as (b) but for S. China. **f** Same as (c) but for S. China. In each region, $\delta^{18}\text{O}_p = \Delta_{dP_{Ont}} + \Delta_{d\delta}$. PO the Pacific Ocean, IO the Indian Ocean, AO the Atlantic Ocean, EAS East Asia Continent, EC the Eurasian Continent, Other, the remaining other tagging regions. The bold black line in each panel represents the total $\delta^{18}\text{O}_p$ anomaly, $\Delta_{dP_{Ont}}$, or $\Delta_{d\delta}$ for each study regions.

isotope change from the source region (see Methods, Part 3). This decomposition illustrates that the AO determines the seasonal $\delta^{18}\text{O}_p$ anomalies in northern China through the $\Delta_{dP_{Ont}}$ component (Fig. 2b, c). This is because, in comparison with local EAS enriched $\delta^{18}\text{O}_p$, the AO's contribution to EAM $\delta^{18}\text{O}_p$ is severely depleted ($\sim -5\text{‰}$ vs -30‰ , Supplementary Fig. 2c), as moisture travels long distances across the Eurasian Continent, undergoing upstream rainout. In winter, the AO is a major oceanic moisture source for northern China, accounting for over 20% of precipitation (Supplementary Fig. 2a), leading to $\delta^{18}\text{O}_p$ depletion. In summer, as the AO's contribution diminishes (Supplementary Fig. 2a) due to the northward migration of the westerly jet and the increased source from the nearby EAS (where the $\delta^{18}\text{O}_p$ is enriched $\sim -6\text{‰}$, Supplementary Fig. 2c), the $\delta^{18}\text{O}_p$ anomaly returns to positive. This seasonal change in the AO moisture contribution causes $\delta^{18}\text{O}_p$ to be negative in winter and positive in summer (Fig. 2a, b). It should be noted that the $\Delta_{d\delta}$ component from the Pacific Ocean (PO) contributes to the “temperature effect” in northern China (Fig. 2a, c). However, the offsetting effects of the $\Delta_{d\delta}$ and $\Delta_{dP_{Ont}}$ from the PO result in a negligible seasonal variation in $\delta^{18}\text{O}_p$ change induced by the PO (Fig. 2a–c). Consequently, the seasonal $\delta^{18}\text{O}_p$ anomaly in northern China is primarily driven by the $\Delta_{dP_{Ont}}$ component from the AO (Fig. 2a–c). We emphasize the significant role of the AO in winter precipitation in northern China, which has not been widely recognized in previous studies using other approaches like the Lagrangian method^{51,52}. The Lagrangian method infers moisture sources based on the evaporation-precipitation difference assumptions^{51,52}, whereas our water tagging method can directly trace moisture sources where evaporation occurs and unaffected by precipitation events^{18,53}. Additionally, the Lagrangian method is restricted by several other assumptions and limitations, notably the exclusion of important processes like convection, turbulence, and numerical diffusion⁵². In essence, for Lagrangian methods to be reliable, they require high-frequency observational data and an integration period longer than 10 days

for the calculations⁵⁴. In contrast, the water-tagging approach accounts for complex feedbacks (e.g., cloud microphysics) and offers a comprehensive view of moisture contributions and isotopic evolution under varying climate conditions^{15,18}. We assert that the water tagging method implemented in the iCAM5.3 model is reliable, as it accurately reproduces the seasonal cycle of $\delta^{18}\text{O}_p$ in North China (Fig. 1f).

In contrast, the $\Delta_{dP_{Ont}}$ from the remote Indian Ocean (IO) is the major factor driving the apparent “amount effect” in southern China (Fig. 2d–f). Southern China is influenced by two major moisture sources, the IO and PO (Supplementary Fig. 2b). The IO has more depleted $\delta^{18}\text{O}_p$ ($\sim -15\text{‰}$ annually) due to its longer distance to reach southern China (Supplementary Fig. 2d). In winter, the IO's contribution is small, and the $\delta^{18}\text{O}_p$ in southern China is dominated by the relatively enriched PO contribution ($\sim -8\text{‰}$ annually). However, in summer, the IO's contribution increases significantly and becomes comparable to that of the PO (Supplementary Fig. 2b). As a result, in southern China, there is a negative $\delta^{18}\text{O}_p$ anomaly in summer and a positive anomaly in winter (Fig. 2d). The importance of the IO for southern China aligns with previous study that has investigated $\delta^{18}\text{O}_p$ variations between summer and winter seasons¹⁵. Overall, the $\Delta_{d\delta}$ component does not influence the seasonal $\delta^{18}\text{O}_p$ anomaly in southern China (Fig. 2d, f).

Our analysis reveals a consistent mechanism behind the contrasting seasonal $\delta^{18}\text{O}_p$ variations in northern China and southern China. These variations are primarily dictated by changes from the remote moisture sources of the AO and IO ($\Delta_{dP_{Ont}}$, Fig. 2b, e), rather than by local temperature and precipitation amount. Additionally, $\Delta_{dP_{Ont}}$ consistently serves as the main factor driving the seasonal variations of $\delta^{18}\text{O}_p$ in the EAM region under climate conditions that differ significantly from the PI climate (Supplementary Fig. 3; Supplementary Fig. 4). However, the differences in the seasonal amplitude of $\delta^{18}\text{O}_p$ across climate conditions are not necessarily driven by $\Delta_{dP_{Ont}}$. For example, in northern China, the

increase in the seasonal amplitude of $\delta^{18}\text{O}_p$ during periods of enhanced summer insolation (P_{\min}) is primarily due to $\Delta_{\delta_{\text{Enroute}}}$ rather than $\Delta_{\text{dP}_{\text{Ori}}}$ (Supplementary Fig. 3a, e).

Enroute depletion ($\Delta_{\delta_{\text{Enroute}}}$) dominates the seasonal change of isotope value Δ_{δ}

Although the isotope value change Δ_{δ} is not the dominant factor in the seasonal cycle of $\delta^{18}\text{O}_p$, we briefly discuss it here for comparison with $\delta^{18}\text{O}_p$ variability on longer timescales later. We decompose the seasonal Δ_{δ} change into three sub-processes associated with the changes over the source region, the enroute process, and the condensation over the sink region: $\Delta_{\delta} = \Delta_{\delta_{\text{Source}}} + \Delta_{\delta_{\text{Enroute}}} + \Delta_{\delta_{\text{Condensation}}}$ (see Methods, Part 3). Our decomposition analysis reveals that the seasonal Δ_{δ} in both northern China and southern China is mainly driven by changes in the enroute depletion process $\Delta_{\delta_{\text{Enroute}}}$. For northern China, the seasonal anomaly of Δ_{δ} is contributed mainly by the enroute process, especially from the PO (Fig. 2c; Supplementary Fig. 5a–c). A further analysis shows this enroute contribution from the PO is dominated by that from the subtropical North Pacific (SNP) (Supplementary Fig. 6). The seasonal changes in SNP $\Delta_{\delta_{\text{Enroute}}}$ are influenced by the north-south movement of the low-latitude circulation. From winter to summer, the North Pacific Subtropical High migrates northward, and the southern branch of its anticyclonic circulation transports moisture from the SNP to northern China via a shorter path in summer than winter (Supplementary Fig. 7). As a result, the values of water vapor ($\delta^{18}\text{O}_v$) arriving in North China are enriched in summer than winter ($\sim -20\%$ vs -60% , Supplementary Fig. 8a). This causes the enrichment in summer and depletion in winter of the PO $\Delta_{\delta_{\text{Enroute}}}$ (Supplementary Fig. 5b). Relatively, the seasonal changes in $\delta^{18}\text{O}_v$ arriving in southern China from SNP are less pronounced (Supplementary Fig. 8b). The longer summer moisture transport path from the IO may explain why SNP $\delta^{18}\text{O}_v$ peaks in spring rather than summer in southern China (-15% vs -16.6% , Supplementary Fig. 7a, b; Supplementary Fig. 8b).

Competition between moisture source ($\Delta_{\text{dP}_{\text{Ori}}}$) and enroute depletion ($\Delta_{\delta_{\text{Enroute}}}$) determining $\delta^{18}\text{O}_p$ on longer timescales

We now further examine the mechanisms underlying $\delta^{18}\text{O}_p$ variations in northern and southern China on longer timescales, comparing them with the seasonal cycle. Analogous to the seasonal cycle study, $\delta^{18}\text{O}_p$ changes can be better understood as the difference between two time periods using a decomposition. This study advances previous work by developing a refined decomposition method that separates the precipitation seasonality component from the moisture source component (see Methods, Part 4). This approach is particularly valuable, as previous studies have highlighted the potential influence of precipitation seasonality on $\delta^{18}\text{O}_p$ in East Asia^{23,35,46–50}. In our method, the change of $\delta^{18}\text{O}_p$ can be decomposed into three components: the change of precipitation seasonality $\Delta_{\text{dP}_{\text{Ori}}}$, the change of moisture source $\Delta_{\text{dP}_{\text{Ori}}}$, and the change of isotope values Δ_{δ} . The Δ_{δ} can be further decomposed into three processes: the source change $\Delta_{\delta_{\text{Source}}}$, enroute change $\Delta_{\delta_{\text{Enroute}}}$, and condensation change $\Delta_{\delta_{\text{Condensation}}}$ (see Methods, Part 4). The decomposition analysis shows that the precipitation seasonality $\Delta_{\text{dP}_{\text{Ori}}}$ is not important for $\delta^{18}\text{O}_p$ changes in the EAM region on millennial and orbital timescales, unlike high-latitude regions such as Greenland^{55,56}. Instead, $\delta^{18}\text{O}_p$ changes are primarily determined by the competition between the changes of moisture source $\Delta_{\text{dP}_{\text{Ori}}}$ and the changes in isotope values via the enroute process $\Delta_{\delta_{\text{Enroute}}}$ (Fig. 3).

On millennial timescales, we examine the $\delta^{18}\text{O}_p$ change from the Last Glacial Maximum (LGM) to Heinrich Stadial 1 (HS1). Both observational and model data show a spatially coherent positive $\delta^{18}\text{O}_p$ change across the pan Asian monsoon region in the HS1–LGM difference (Fig. 3a), aligning with previous studies^{18,53}. In contrast, the annual precipitation anomaly exhibits a heterogeneous response: significant increase in southern China and a decrease across the Indian monsoon region (Supplementary Fig. 9a). Therefore, $\delta^{18}\text{O}_p$ and rainfall anomalies are both positive in southern China, which does not align with the classical “amount effect”. Our decomposition analysis shows that positive $\delta^{18}\text{O}_p$ variations in both northern and southern

China are primarily result from the enroute process $\Delta_{\delta_{\text{Enroute}}}$, which alters the isotope values in Δ_{δ} (Fig. 3b, c). There is minimal contribution from $\Delta_{\text{dP}_{\text{Ori}}}$ or $\Delta_{\text{dP}_{\text{Sea}}}$ (Fig. 3b, c). The dominant process is the $\Delta_{\delta_{\text{Enroute}}}$ change associated with the IO, rather than the PO, which dominates the $\Delta_{\delta_{\text{Enroute}}}$ changes on seasonal timescales (Supplementary Fig. 5b, e). Mechanistically, during HS1, the weakening of the Indian summer monsoon shortens the moisture transport distance from the Indian Ocean to EAM region (Supplementary Fig. 10a, b; Supplementary Fig. 11). This shortened distance results in a positive $\delta^{18}\text{O}_p$ variation across the EAM region due to reduced enroute isotopic depletion^{18,53}. This mechanism differs significantly from the seasonal cycle, which is dominated by seasonal change of moisture source $\Delta_{\text{dP}_{\text{Ori}}}$ in the EAM region, as discussed earlier (Fig. 2b, e). Additionally, the $\Delta_{\delta_{\text{Source}}}$ and $\Delta_{\delta_{\text{Condensation}}}$ also contribute to the positive $\delta^{18}\text{O}_p$ variations, especially in northern China, due to reduced upstream rainout (Supplementary Fig. 9a) and enhanced local EAS contribution (Fig. 3b, c, refs. 18,53).

On orbital timescales, we investigate the $\delta^{18}\text{O}_p$ responses to two different precessional forcing: one with minimum precession (P_{\min}) and the other with maximum precession (P_{\max}). Our model simulations, along with previous observations, reveal a spatially coherent negative $\delta^{18}\text{O}_p$ variation across the Indian monsoon region to northern China during the transition from reduced (P_{\max}) to intensified (P_{\min}) summer insolation (Fig. 3d). This finding is consistent with results from previous modeling studies^{15,57,58}. In contrast, the precipitation amount response to orbital forcing shows a north-south dipole pattern, with increasing precipitation in northern China and decreasing precipitation in southern China (Supplementary Fig. 9b). Therefore, the $\delta^{18}\text{O}_p$ anomaly in northern China aligns with the “amount effect”, but this is not the case in southern China, consistent with previous work¹². The negative $\delta^{18}\text{O}_p$ response is primarily caused by the changes of moisture source $\Delta_{\text{dP}_{\text{Ori}}}$ in both northern and southern China (Fig. 3e, f). Mechanistically, intensified summer insolation during P_{\min} increases the transport of moisture from the remote PO and IO (Supplementary Fig. 10c), both of which contribute highly depleted isotope values to northern China (Fig. 3e, f). This lead to significant $\delta^{18}\text{O}_p$ depletion, as indicated by the negative $\Delta_{\text{dP}_{\text{Ori}}}$ (Fig. 3e, f). In southern China, the increased moisture from the remote PO is partially offset by the reduced moisture from the IO, resulting in less significant $\delta^{18}\text{O}_p$ depletion in $\Delta_{\text{dP}_{\text{Ori}}}$ (Fig. 3f; Supplementary Fig. 10d). Although the enroute process $\Delta_{\delta_{\text{Enroute}}}$ contributes the most to depletion in southern China, this contribution is largely offset by the condensation process $\Delta_{\delta_{\text{Condensation}}}$, leading to a negligible total contribution from the isotope value response Δ_{δ} . Therefore, the dominant impact comes from the $\Delta_{\text{dP}_{\text{Ori}}}$ (Fig. 3f). Previous studies have suggested that the orbital-scale $\delta^{18}\text{O}_p$ variation in southern China is primarily influenced by the IO, based on seasonal timescales findings¹⁵. However, our study reveals the PO's primary influence on East Asian $\delta^{18}\text{O}_p$ on orbital timescales, contrasting with the seasonal and millennial scales, which are dominated by the IO. This suggest that a simplistic comparison between seasonal and precessional timescales warrants additional scrutiny and discussion. Previous studies have shown that orbital-scale $\delta^{18}\text{O}_p$ variations in the Indian monsoon region are also linked to changes in moisture source $\Delta_{\text{dP}_{\text{Ori}}}$ ⁵⁷. This implies a consistent mechanism for $\delta^{18}\text{O}_p$ variation across the Asian monsoon region on orbital timescales: intensified summer insolation strengthens the monsoon, driving more remote moisture to the region and resulting in a uniform $\delta^{18}\text{O}_p$ depletion across the entire Asian monsoon region. This consistent mechanism is further supported by a recent model study across the Asian monsoon region⁵⁸.

Our decomposition analysis reveals that the $\delta^{18}\text{O}_p$ variations across the EAM region are primarily driven by enroute depletion $\Delta_{\delta_{\text{Enroute}}}$ on millennial timescales, while changes in moisture source $\Delta_{\text{dP}_{\text{Ori}}}$ on orbital timescales. Unlike the season cycle, the AO plays a negligible role in influencing the $\delta^{18}\text{O}_p$ variations in northern China on millennial and orbital timescales. This difference arises because annual $\delta^{18}\text{O}_p$ in northern China is dominated by the $\delta^{18}\text{O}_p$ change during summer monsoon season (Supplementary Fig. 1e), while the AO plays a stronger role only in winter (Supplementary Fig. 1a). Instead, in summer, both northern and southern China experience significant precipitation from moisture sources in the IO and PO

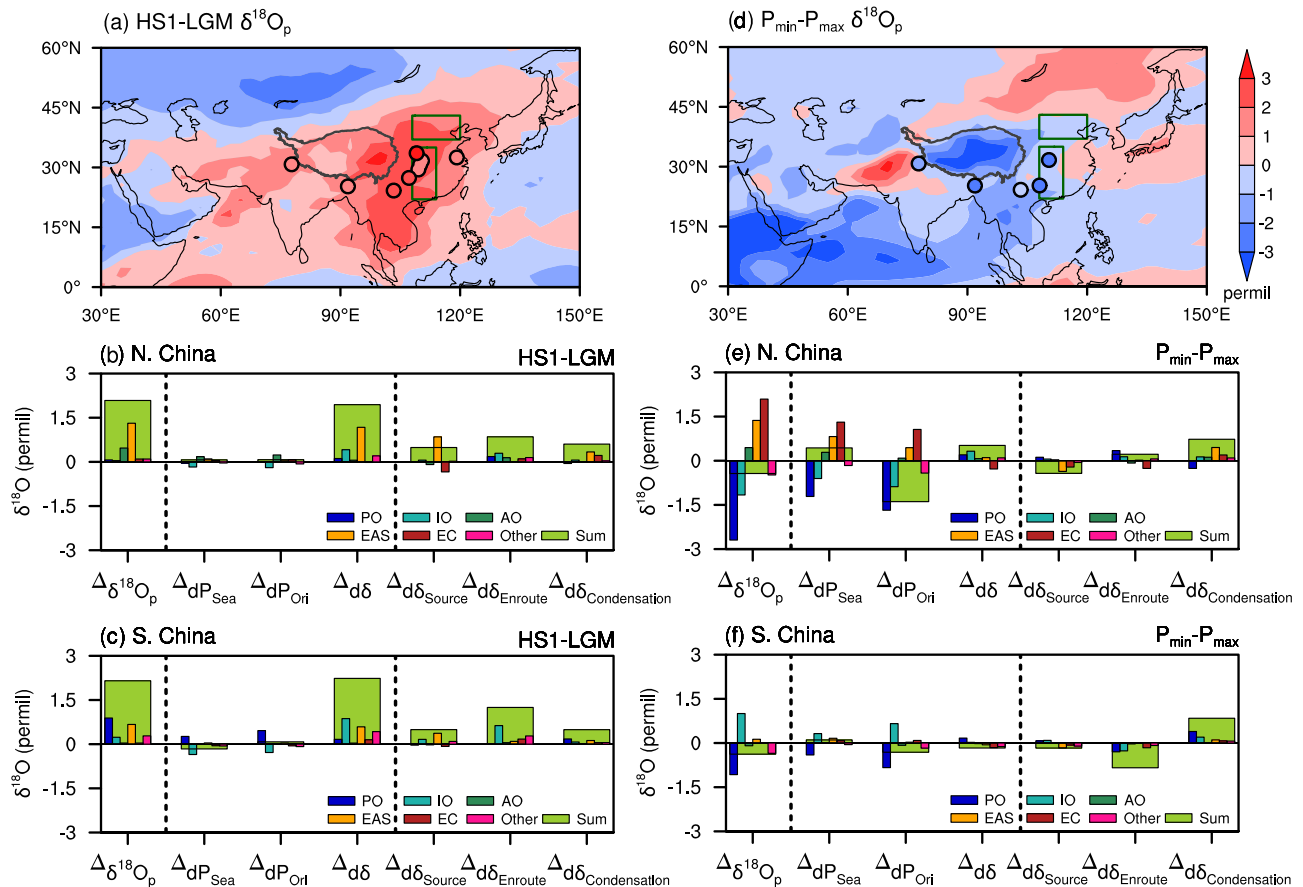


Fig. 3 | $\delta^{18}\text{O}_p$ variations and its decomposition on millennial and orbital timescales in N. China and S. China. **a** The $\delta^{18}\text{O}_p$ difference between HS1 and LGM across the pan-Asian monsoon region. **b** The $\delta^{18}\text{O}_p$ difference between HS1 and LGM and its decomposition in N. China. **c** The $\delta^{18}\text{O}_p$ difference between HS1 and LGM and its decomposition in S. China. **d** The $\delta^{18}\text{O}_p$ difference between P_{\min} and P_{\max} across the pan-Asian monsoon region. **e** The $\delta^{18}\text{O}_p$ difference between P_{\min} and P_{\max} and its decomposition in N. China. **f** The $\delta^{18}\text{O}_p$ difference between P_{\min} and P_{\max} and its decomposition in S. China. In this figure, $\delta^{18}\text{O}_p$ represents the precipitation-weighted annual $\delta^{18}\text{O}_p$. In (a, d), solid circles represent observed cave

speleothem $\delta^{18}\text{O}$ records (Supplementary Table 2). Note that our study focuses on the western part of S. China (22°N to 35°N , 108°E to 114°E) on millennial and orbital timescales, where model results are consistent with observations on orbital timescales. The dark gray lines outline the Tibetan Plateau boundary. In (b, c, e, f), $\Delta\delta^{18}\text{O}_p = \Delta dP_{\text{Sea}} + \Delta dP_{\text{Ori}} + \Delta d\delta$, and $\Delta d\delta = \Delta d\delta_{\text{Source}} + \Delta d\delta_{\text{Enroute}} + \Delta d\delta_{\text{Condensation}}$. PO the Pacific Ocean, IO the Indian Ocean, AO the Atlantic Ocean, EAS East Asia Continent, EC the Eurasian Continent, Other, the remaining other tagging regions. The Sum in each panel represents the total $\Delta\delta^{18}\text{O}_p$, ΔdP_{Sea} , ΔdP_{Ori} , $\Delta d\delta_{\text{Source}}$, $\Delta d\delta_{\text{Enroute}}$, or $\Delta d\delta_{\text{Condensation}}$ of six tagging domains.

(Supplementary Fig. 1e, f). As a result, their annual $\delta^{18}\text{O}_p$ exhibit synchronous responses to the influences of the IO or PO influences on millennial and orbital timescales, mediated by enroute depletion $\Delta d\delta_{\text{Enroute}}$ and moisture source ΔdP_{Ori} (Fig. 3b, c, e, f). This explains why consistent $\delta^{18}\text{O}_p$ variations are observed on millennial and orbital timescales in the EAM region, but are absent on the seasonal timescales.

The framework we developed emphasizes the distinction in $\delta^{18}\text{O}_p$ variations across seasonal and longer timescales, highlighting that longer timescales are additionally influenced by precipitation seasonality. When precipitation seasonality is not significant for a specific region, the $\delta^{18}\text{O}_p$ variations on different timescales in this region can be explained through our framework, which isolates and quantifies the relative contributions of different water cycle processes. This refined $\delta^{18}\text{O}_p$ decomposition method in our study can be generalized to other monsoon systems, such as the South Asian⁵⁷ and African monsoons⁵⁹, as well as to various paleoclimate archives, including ice cores⁵⁶, tree rings, and lake sediments. The broad application of this method will greatly enhance our understanding of the climatic significance of $\delta^{18}\text{O}_p$ at different timescales across different regions.

Conclusions

The contrasting $\delta^{18}\text{O}_p$ response across the EAM region on seasonal timescales and the coherent $\delta^{18}\text{O}_p$ response on millennial and orbital timescales can be understood through a unified framework as caused by different

mechanisms, notably the competition between the change of moisture sources and the enroute depletion. The seasonal contrast in $\delta^{18}\text{O}_p$ between northern and southern China is primarily caused by the shifts in moisture sources: the very depleted $\delta^{18}\text{O}_p$ from the remote AO in winter for northern China and from the remote IO in summer for southern China (Fig. 4a). On millennial timescales, the coherent $\delta^{18}\text{O}_p$ response across the entire EAM region results from similar isotope enrichment from the major moisture source of the IO, via the enroute process, along with reduced upstream precipitation linked to a weakening summer monsoon in response to meltwater forcing (Fig. 4b). On orbital timescales, the coherent $\delta^{18}\text{O}_p$ response is mainly caused by a stronger summer monsoon, which transports more depleted moisture from the PO or IO moisture to the EAM region (Fig. 4c). In none of the cases, the change of $\delta^{18}\text{O}_p$ is directly related to the change of local temperature and precipitation amount. Our study highlights that the correlation between $\delta^{18}\text{O}_p$ and local meteorological factors on a seasonal scale should not be directly applied to interpret longer-term isotopic variability in paleoclimate proxies, even qualitatively. Instead, long-term $\delta^{18}\text{O}_p$ variations in East Asia are primarily influenced by changes in moisture source and enroute processes, two key components of the summer monsoon system associated with seasonal precipitation reversals and meridional shifts in low-latitude circulation, respectively⁶⁰.

Observational records suggest that $\delta^{18}\text{O}_p$ variations in the EAM region on decadal- to centennial-scale do not exhibit a robust coherent or north-

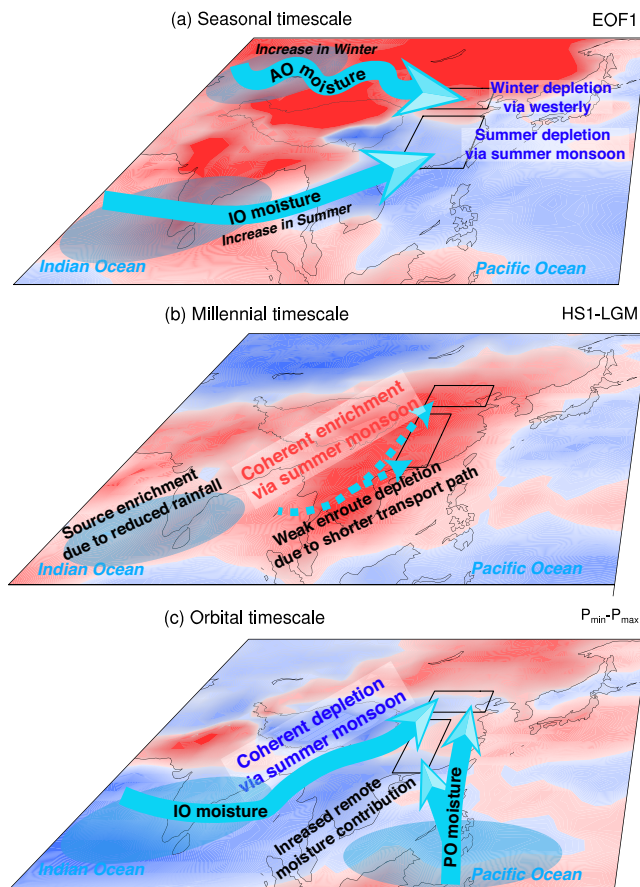


Fig. 4 | Schematic diagrams illustrating $\delta^{18}\text{O}_p$ variations across timescales in the EAM region. a Seasonal timescale. In summer, the monsoon carries remote IO moisture to S. China, depleting $\delta^{18}\text{O}_p$ in this region. In winter, westerly winds bring remote AO moisture to N. China, depleting $\delta^{18}\text{O}_p$ here. **b** Millennial timescales. During HS1, a weakened Indian summer monsoon increases transport of nearby IO moisture (e.g., the Bay of Bengal) to the EAM region. Reduced enroute depletion enriches $\delta^{18}\text{O}_p$ across the EAM region. **c** Orbital timescales. During P_{min}, intensified insolation enhances remote PO moisture transport to the EAM region, depleting $\delta^{18}\text{O}_p$ across the EAM region. Notably, the remote IO also contributes to the depleted $\delta^{18}\text{O}_p$ in N. China but not in S. China due to reduced IO contribution there. Blue shading in each panel represents $\delta^{18}\text{O}_p$ depletion while red shading represents $\delta^{18}\text{O}_p$ enrichment. PO the Pacific Ocean, IO the Indian Ocean, AO the Atlantic Ocean. HS1 the Heinrich Stadial I (15.5 ka BP). LGM the Last Glacial Maximum (20 ka BP). P_{min} Precessional minimum (127 ka BP). P_{max} Precessional maximum (116 ka BP).

south dipole patterns^{15,61–65}. This inconsistency may indicate the important influence of local factors, independent of the monsoon system, on $\delta^{18}\text{O}$ variations on these timescales. Such local factors fall outside the scope of this study, which focuses on the monsoon-related mechanisms driving $\delta^{18}\text{O}_p$ variability across the EAM region. Additionally, a systematic, multi-model investigation into the effects of moisture source and enroute depletion on $\delta^{18}\text{O}_p$ variations across different timescales in the EAM region would provide a more comprehensive and robust understanding of how summer monsoon evolution is reflected in oxygen isotope records.

Methods

Part 1: Precipitation stable isotope data

We used observational monthly $\delta^{18}\text{O}_p$ data from 24 stations located in the East Asian monsoon (EAM) region and its surrounding areas, sourced from the Global Network of Isotopes in Precipitation (GNIP). The stations were selected based on the availability of complete monthly data after multiyear averaging (Supplementary Table 1).

Part 2: Water tagging experiments

Recently, researchers have utilized water tagging methods in numerical models to examine changes in $\delta^{18}\text{O}_p$ in the EAM region^{15,18,31}. The tagging experiment is designed to trace the life cycle of water isotopes. H_2^{16}O or H_2^{18}O is traced from the tagging region once it evaporates from the surface (source region) and follows the hydrological cycle in the model to the region where it rains out (sink region). We performed five snapshot water tagging experiments during the pre-industrial (PI), Heinrich Stadial 1 (HS1, 15.5 ka BP), Last Glacial Maximum (LGM, 20 ka BP), precessional minimum (P_{min}, 127 ka BP), and precessional maximum (P_{max}, 116 ka BP) periods using the isotope-enabled Community Atmosphere Model (iCAM5.3), the atmospheric model in iCESM1.3. We use the “FV2” version of the iCESM1.3, which employs a finite-volume dynamical core at a nominal resolution of 2° . The iCAM5.3 has a horizontal resolution of 1.9° in latitude and 2.5° in longitude, and a vertical resolution of 30 levels. The isotopic ratios, related fluxes, and isotope fractionation are simulated across all components of the hydrological cycle. The tagging experiments for the PI, HS1, and LGM periods were driven by sea ice distribution, sea surface temperature, and sea surface $\delta^{18}\text{O}$ data from the iCESM1.3 experiment, which is an isotope-enabled full forcing transient climate experiment including icesheet, orbital, greenhouse gas, and meltwater forcing. Detailed experiment setup descriptions can be obtained from refs. 18,56. The forcing for the two water tagging experiments, named P_{min} and P_{max}, are directly derived from a 100-fold accelerated single-orbit forced transient simulation of the past 300 ka⁵⁸. In this transient experiment, all boundary conditions are kept fixed in the PI period, with only changes made to the Earth’s orbital parameters. The direct model-data comparison demonstrates that the model can effectively simulate the $\delta^{18}\text{O}_p$ variations in the East Asian monsoon (EAM) region during the last deglaciation, including the LGM and HS1 periods¹⁸. Furthermore, the model also accurately captures the $\delta^{18}\text{O}_p$ variations in the EAM region over the past 300,000 years, particularly during the precession cycle⁵⁸.

Of the five water tagging experiments, the PI experiment is utilized to analyze the seasonal $\delta^{18}\text{O}_p$ variations in the EAM region. Millennial-scale abrupt climate changes, characterized by rapid transitions between cold stadial and warm interstadial states, are most prevalent during glacial periods^{67,68}. HS events, driven by extreme ice-rafting, represent the coldest of these stadials⁵³ and are recorded in speleothem $\delta^{18}\text{O}$ records in the EAM regions⁶⁹. In this study, the modeled millennial-scale $\delta^{18}\text{O}_p$ changes are primarily attributed to meltwater forcing¹⁸. Therefore, we focused on the HS1-LGM period of the last deglaciation to analyze millennial-scale $\delta^{18}\text{O}_p$ variations, as this interval was characterized by relatively small changes in ice sheets, greenhouse gases, and orbital parameters, allowing us to better isolate the impact of meltwater forcing. The pervasive millennial-scale abrupt climate changes during glacial-interglacial cycles⁷⁰ are often linked to changes in the Atlantic Meridional Overturning Circulation (AMOC) induced by meltwater forcing^{71,72}. Therefore, while the HS1-LGM transition provides a valuable case study of deglacial millennial-scale climate change, it also offers insights into the mechanisms driving similar $\delta^{18}\text{O}_p$ variations during other abrupt climate events, including warm interglacial periods. While obliquity-induced changes in insolation are considered to impact East Asian seasonality and monsoons at orbital scales⁷³, the monsoon’s response to obliquity forcing is weaker than its response to precession forcing⁷⁴. For $\delta^{18}\text{O}$ variations in this study, observations show that the most prominent cycle in speleothem $\delta^{18}\text{O}$ records in the EAM region is the ~20,000-year precession cycle⁶⁹. Our simulations also reveal a clear precession cycle in $\delta^{18}\text{O}_p$ for both South and North China, with no indication of a ~40,000-year obliquity cycle (Supplementary Fig. 12). A previous study demonstrated that even after removing the precessional component, the variance within the precessional band in the detrended (suborbital) speleothem $\delta^{18}\text{O}$ signal still exceeds that within the obliquity band, indicating a minor role for obliquity⁶⁹. Therefore, the P_{min} and P_{max} experiments are used for analyzing variations on orbital timescales. The simulation result shows a subtle increase in $\delta^{18}\text{O}_p$ values in southeastern China during P_{min} when insolation intensifies (Fig. 3d). This result contradicts the speleothem $\delta^{18}\text{O}$ records

reported in previous studies conducted at Hulu Cave (32.50°N, 119.17°E)^{75,76}. To address this discrepancy, we conducted a decomposition analysis specifically targeting the millennial and orbital variations in $\delta^{18}\text{O}_p$ in southwestern China (22°N to 35°N, 108°E to 114°E), where simulation results align with observations (Fig. 3d). In addition, the P_{\min} and P_{\max} experiments exclude changes in ice sheets, greenhouse gases, meltwater forcing, and seawater isotopes, which may explain why the simulated $\delta^{18}\text{O}_p$ amplitudes are smaller than the observed variations (Fig. 3d). However, they effectively capture the general $\delta^{18}\text{O}_p$ changes across the southwestern China and northern China driven by precession-cycle insolation (Fig. 3d). This makes these experiments well-suited for investigating the mechanisms driving $\delta^{18}\text{O}_p$ changes in the EAM region on precession timescale, which is the primary focus of this study. This study does not analyze time scales ranging from a decade to a century, based on two main considerations. First, on these time scales, the $\delta^{18}\text{O}$ records in the EAM region do not show consistent spatial patterns. Specifically, the $\delta^{18}\text{O}$ variations in southern and northern China differ significantly¹⁹; even within southern China, there are large differences in $\delta^{18}\text{O}$ records between different sites⁷⁷. This makes it difficult to extract a clear regional $\delta^{18}\text{O}$ periodic signal on these time scales, and it becomes even harder to analyze its underlying mechanisms. On the other hand, the model's ability to simulate these time scales requires further verification. Previous results indicate that the iCESM model can simulate large-scale drought conditions from the Medieval Climate Anomaly (MCA) to the Little Ice Age (LIA), but it fails to capture the temporal evolution of the climate recorded in proxy over the Common Era⁷⁸. A recent model-data comparisons over the past millennium using multiple isotope-enabled climate models underscore the difficulty of reliably validating model simulations on decadal to centennial scales using speleothem isotope records due to the lower temporal resolution of speleothem records, karst mixing effects, and uncertainties in volcanic forcing reconstructions⁷⁹. Thus, applying decomposition approach to investigate the $\delta^{18}\text{O}_p$ variability across these timescales remains a task for future research.

We employ 25 tags globally and each tag utilizes either oceanic evaporation or land evapotranspiration (Supplementary Fig. 13). This tagging methods are different from previous modern studies that mainly focus on the effects of several main moisture source on $\delta^{18}\text{O}_p$ variations in the EAM region^{15,31}. In our work, the total monthly precipitation amount (P_m) and precipitation water isotope ratio ($\delta^{18}\text{O}_{p,m}$) for a specific region can be calculated using the following equations:

$$P_m = \sum_{i=1}^{25} P_{i,m}, \quad m = 1, 2, 3, \dots, 12 \quad (1a)$$

$$\delta^{18}\text{O}_{p,m} = \sum_{i=1}^{25} \delta^{18}\text{O}_{p,i,m} \left(\frac{P_{i,m}}{P_m} \right), \quad m = 1, 2, 3, \dots, 12 \quad (1b)$$

where $P_{i,m}$ (or $\delta^{18}\text{O}_{p,i,m}$) refers to the precipitation amount (or $\delta^{18}\text{O}$) contribution of tagging region i in a given month m .

Part 3: Decomposing seasonal $\delta^{18}\text{O}_p$ variations

The seasonal $\delta^{18}\text{O}_{p,m}$ anomaly ($\Delta\delta^{18}\text{O}_{p,m}$) is its difference from the annual mean $\delta^{18}\text{O}_p$

$$\delta^{18}\text{O}_{p,a} = \frac{\sum_{j=1}^{12} \sum_{i=1}^{25} \delta^{18}\text{O}_{p,i,j} \left(\frac{P_{i,j}}{P_j} \right)}{12}, \quad (2)$$

as

$$\Delta\delta^{18}\text{O}_{p,m} = \delta^{18}\text{O}_{p,m} - \delta^{18}\text{O}_{p,a}, \quad m = 1, 2, 3, \dots, 12 \quad (3a)$$

This seasonal change $\Delta\delta^{18}\text{O}_{p,m}$ in the sink region reflects the contributions from all source regions. Using Eqs. (1b) and (2), this seasonal $\Delta\delta^{18}\text{O}_{p,m}$ can be decomposed into two parts. The first part is the contribution to the precipitation weight change from different source regions,

or simply moisture source change $\Delta\delta^{18}\text{O}_{p,\text{On}}$, and the second part associated with the change of the $\delta^{18}\text{O}_p$ value from different source regions, or simply isotope change $\Delta\delta_6$ (Supplementary Fig. 14a).

$$\Delta\delta^{18}\text{O}_{p,m} = \Delta\delta^{18}\text{O}_{p,\text{On}} + \Delta\delta_6, \quad m = 1, 2, 3, \dots, 12 \quad (3b)$$

with each part contributed by that from all source regions as

$$\Delta\delta^{18}\text{O}_{p,\text{On}} = \sum_{i=1}^{25} \Delta\delta^{18}\text{O}_{p,\text{On},i}, \quad \Delta\delta^{18}\text{O}_{p,\text{On},i} = \frac{\sum_{j=1}^{12} \frac{1}{2} (\delta^{18}\text{O}_{p,i,j} + \delta^{18}\text{O}_{p,i,m}) \left(\frac{P_{i,m}}{P_m} - \frac{P_{i,j}}{P_j} \right)}{12} \quad (3c)$$

$$\Delta\delta_6 = \sum_{i=1}^{25} \Delta\delta_{6,i}, \quad \Delta\delta_{6,i} = \frac{\sum_{j=1}^{12} \frac{1}{2} \left(\frac{P_{i,j}}{P_j} + \frac{P_{i,m}}{P_m} \right) (\delta^{18}\text{O}_{p,i,m} - \delta^{18}\text{O}_{p,i,j})}{12} \quad (3d)$$

The isotope change, from say, region i , $\Delta\delta_{6,i}$ can be further decomposed along its trajectory to three processes: source process $\Delta\delta_{6,i,\text{Source}}$, enroute process $\Delta\delta_{6,i,\text{Enroute}}$, and condensation process $\Delta\delta_{6,i,\text{Condensation}}$ ⁵⁷. Hence, the $\Delta\delta_{6,i}$ term in equation (3d) can be further decomposed using vapor water isotope $\delta^{18}\text{O}_v$ into three components (Supplementary Fig. 14a):

$$\Delta\delta_{6,i} = \Delta\delta_{6,i,\text{Source}} + \Delta\delta_{6,i,\text{Enroute}} + \Delta\delta_{6,i,\text{Condensation}}, \quad (4a)$$

where

$$\Delta\delta_{6,i,\text{Source}} = \sum_{j=1}^{12} \frac{1}{2} \left(\frac{P_{i,j}}{P_j} + \frac{P_{i,m}}{P_m} \right) \Delta(\delta^{18}\text{O}_{v,\text{Source}}), \quad (4b)$$

$$\Delta(\delta^{18}\text{O}_{v,\text{Source}}) = \delta^{18}\text{O}_{v,i,m,\text{Source}} - \delta^{18}\text{O}_{v,i,j,\text{Source}}, \quad (4c)$$

$$\Delta\delta_{6,i,\text{Enroute}} = \sum_{j=1}^{12} \frac{1}{2} \left(\frac{P_{i,j}}{P_j} + \frac{P_{i,m}}{P_m} \right) \Delta(\delta^{18}\text{O}_{v,\text{Sink}} - \delta^{18}\text{O}_{v,i,j,\text{Source}}), \quad (4d)$$

$$\Delta(\delta^{18}\text{O}_{v,\text{Sink}} - \delta^{18}\text{O}_{v,i,j,\text{Source}}) = \left(\delta^{18}\text{O}_{v,i,m,\text{Sink}} - \delta^{18}\text{O}_{v,i,j,\text{Sink}} \right) - \left(\delta^{18}\text{O}_{v,i,m,\text{Source}} - \delta^{18}\text{O}_{v,i,j,\text{Source}} \right), \quad (4e)$$

$$\Delta\delta_{6,i,\text{Condensation}} = \sum_{j=1}^{12} \frac{1}{2} \left(\frac{P_{i,j}}{P_j} + \frac{P_{i,m}}{P_m} \right) \Delta(\delta^{18}\text{O}_{p,i} - \delta^{18}\text{O}_{v,i,j,\text{Sink}}), \quad (4f)$$

$$\Delta(\delta^{18}\text{O}_{p,i} - \delta^{18}\text{O}_{v,i,j,\text{Sink}}) = \left(\delta^{18}\text{O}_{p,i,m} - \delta^{18}\text{O}_{p,i,j} \right) - \left(\delta^{18}\text{O}_{v,i,m,\text{Sink}} - \delta^{18}\text{O}_{v,i,j,\text{Sink}} \right), \quad (4g)$$

In Eqs. (4b)–(4g), m represents a specific month of interest, whereas j is a monthly index that iterates from 1 to 12, used to derive the annual average of $\delta^{18}\text{O}_p$. Finally, the seasonal $\delta^{18}\text{O}_p$ anomalies ($\Delta\delta^{18}\text{O}_{p,m}$) are ultimately decomposed into four components: $\Delta\delta^{18}\text{O}_{p,\text{On}}$, $\Delta\delta_{6,\text{Source}}$, $\Delta\delta_{6,\text{Enroute}}$, and $\Delta\delta_{6,\text{Condensation}}$ (Supplementary Fig. 14a).

Part 4: Decomposing $\delta^{18}\text{O}_p$ difference between two periods

We present a refined decomposition method for investigating $\delta^{18}\text{O}_p$ variations on longer timescales. This method decomposes annual $\delta^{18}\text{O}_p$ variations caused by precipitation weight change ($\Delta\delta^{18}\text{O}_p$) into two distinct components: (1) $\delta^{18}\text{O}_p$ variations driven by changes in precipitation seasonality ($\Delta\delta^{18}\text{O}_{p,\text{Sea}}$), and (2) $\delta^{18}\text{O}_p$ variations reflecting changes in moisture source ($\Delta\delta^{18}\text{O}_{p,\text{On}}$). This approach is different from previous studies that combined these two components into a single moisture source component^{15,18,57}. Previous studies have suggested a potential influence of precipitation seasonality on $\delta^{18}\text{O}_p$ in this region^{23,35,46–50}. By isolating these components, our

improved methodology offers a clearer picture of the mechanisms influencing $\delta^{18}\text{O}_p$ variations in East Asia. Specifically, the annual $\delta^{18}\text{O}_p$ difference ($\Delta\delta^{18}\text{O}_{p,a}$) between two periods “1” and “2” can be decomposed into the changes of precipitation seasonality ($\Delta\text{dP}_{\text{Sea}}$) and $\delta^{18}\text{O}_p$ seasonality ($\Delta\text{d}\delta_{\text{Sea}}$) (Supplementary Fig. 14b).

$$\begin{aligned}\Delta\delta^{18}\text{O}_{p,a} &= \delta^{18}\text{O}_{p1,a} - \delta^{18}\text{O}_{p2,a} = \sum_{m=1}^{12} \left(\delta^{18}\text{O}_{p1,m} \frac{P1_m}{P1_a} \right) \\ &- \sum_{m=1}^{12} \left(\delta^{18}\text{O}_{p2,m} \frac{P2_m}{P2_a} \right) = \sum_{m=1}^{12} \left(\left(\frac{P1_m}{P1_a} - \frac{P2_m}{P2_a} \right) \left(\frac{\delta^{18}\text{O}_{p1,m} + \delta^{18}\text{O}_{p2,m}}{2} \right) \right) \\ &+ \sum_{m=1}^{12} \left(\left(\delta^{18}\text{O}_{p1,m} - \delta^{18}\text{O}_{p2,m} \right) \left(\frac{P1_m + P2_m}{2} \right) \right) \quad (5a)\end{aligned}$$

where

$$\frac{P1_m}{P1_a} = \sum_{i=1}^{25} \frac{P1_{m,i}}{P1_a}, \quad (5b)$$

$$\frac{P2_m}{P2_a} = \sum_{i=1}^{25} \frac{P2_{m,i}}{P2_a}, \quad (5c)$$

$$\delta^{18}\text{O}_{p1,m} = \sum_{i=1}^{25} \delta^{18}\text{O}_{p1,m,i} \frac{P1_{m,i}}{P1_m}, \quad (5d)$$

$$\delta^{18}\text{O}_{p2,m} = \sum_{i=1}^{25} \delta^{18}\text{O}_{p2,m,i} \frac{P2_{m,i}}{P2_m}, \quad (5e)$$

Following the decomposition of seasonal $\delta^{18}\text{O}_p$ variations in eqs. (3a–d), water isotope seasonality change $\Delta\text{d}\delta_{\text{Sea}}$ can be further decomposed into $\Delta\text{d}\delta_{\text{Sea}} - \Delta\text{dP}_{\text{Ori}}$ and $\Delta\text{d}\delta_{\text{Sea}} - \Delta\text{d}\delta$ (Supplementary Fig. 14b):

$$\begin{aligned}\Delta\text{d}\delta_{\text{Sea}} &= \sum_{m=1}^{12} \left(\left(\delta^{18}\text{O}_{p1,m} - \delta^{18}\text{O}_{p2,m} \right) \left(\frac{P1_m + P2_m}{2} \right) \right), \\ &= \sum_{m=1}^{12} \left(\left(\sum_{i=1}^{25} \delta^{18}\text{O}_{p1,m,i} \frac{P1_{m,i}}{P1_m} - \sum_{i=1}^{25} \delta^{18}\text{O}_{p2,m,i} \frac{P2_{m,i}}{P2_m} \right) \left(\frac{P1_m + P2_m}{2} \right) \right), \\ &= \sum_{m=1}^{12} \left(\sum_{i=1}^{25} \left(\left(\frac{P1_{m,i}}{P1_m} - \frac{P2_{m,i}}{P2_m} \right) \left(\frac{\delta^{18}\text{O}_{p1,m,i} + \delta^{18}\text{O}_{p2,m,i}}{2} \right) \right) \left(\frac{P1_m + P2_m}{2} \right) \right) \\ &\quad + \sum_{m=1}^{12} \left(\sum_{i=1}^{25} \left(\left(\delta^{18}\text{O}_{p1,m,i} - \delta^{18}\text{O}_{p2,m,i} \right) \left(\frac{P1_{m,i} + P2_{m,i}}{2} \right) \right) \left(\frac{P1_m + P2_m}{2} \right) \right), \quad (6)\end{aligned}$$

Following the seasonal decomposition in Eq. (4a–g), $\Delta\text{d}\delta_{\text{Sea}} - \Delta\text{d}\delta$ can be further decomposed into the processes associated with the source $\Delta\text{d}\delta_{\text{Sea}} - \Delta\text{d}\delta_{\text{Source}}$, enroute $\Delta\text{d}\delta_{\text{Sea}} - \Delta\text{d}\delta_{\text{Enroute}}$ and condensation $\Delta\text{d}\delta_{\text{Sea}} - \Delta\text{d}\delta_{\text{Condensation}}$ as

(Supplementary Fig. 14b)

$$\begin{aligned}\Delta\text{d}\delta_{\text{Sea}} - \Delta\text{d}\delta &= \sum_{m=1}^{12} \left(\sum_{n=1}^{25} \left(\tilde{\Delta}(\delta^{18}\text{O}_{\text{vsource}}) \left(\frac{P1_{m,j} + P2_{m,j}}{2} \right) \right) \left(\frac{P1_m + P2_m}{2} \right) \right) \\ &\quad + \sum_{m=1}^{12} \left(\sum_{n=1}^{25} \left(\tilde{\Delta}(\delta^{18}\text{O}_{\text{vsink}} - \delta^{18}\text{O}_{\text{vsource}}) \left(\frac{P1_{m,j} + P2_{m,j}}{2} \right) \right) \left(\frac{P1_m + P2_m}{2} \right) \right) \\ &\quad + \sum_{m=1}^{12} \left(\sum_{n=1}^{25} \left(\tilde{\Delta}(\delta^{18}\text{O}_p - \delta^{18}\text{O}_{\text{vsink}}) \left(\frac{P1_{m,j} + P2_{m,j}}{2} \right) \right) \left(\frac{P1_m + P2_m}{2} \right) \right) \quad (7a)\end{aligned}$$

where

$$\tilde{\Delta}(\delta^{18}\text{O}_{\text{vsource}}) = \delta^{18}\text{O}_{v1,m,j \text{ source}} - \delta^{18}\text{O}_{v2,m,j \text{ source}} \quad (7b)$$

$$\begin{aligned}\tilde{\Delta}(\delta^{18}\text{O}_{\text{vsink}} - \delta^{18}\text{O}_{\text{vsource}}) &= \left(\delta^{18}\text{O}_{v1,m,j \text{ sink}} - \delta^{18}\text{O}_{v2,m,j \text{ sink}} \right) \\ &- \left(\delta^{18}\text{O}_{v1,m,j \text{ source}} - \delta^{18}\text{O}_{v2,m,j \text{ source}} \right) \quad (7c)\end{aligned}$$

$$\begin{aligned}\tilde{\Delta}(\delta^{18}\text{O}_p - \delta^{18}\text{O}_{\text{vsink}}) &= \left(\delta^{18}\text{O}_{p1,m,j} - \delta^{18}\text{O}_{p2,m,j} \right) \\ &- \left(\delta^{18}\text{O}_{v1,m,j \text{ sink}} - \delta^{18}\text{O}_{v2,m,j \text{ sink}} \right) \quad (7d)\end{aligned}$$

Therefore, the $\Delta\delta^{18}\text{O}_{p,a}$ is decomposed into five components as follows: $\Delta\text{dP}_{\text{Sea}}$, $\Delta\text{d}\delta_{\text{Sea}} - \Delta\text{dP}_{\text{Ori}}$, $\Delta\text{d}\delta_{\text{Sea}} - \Delta\text{d}\delta_{\text{Source}}$, $\Delta\text{d}\delta_{\text{Sea}} - \Delta\text{d}\delta_{\text{Enroute}}$, and $\Delta\text{d}\delta_{\text{Sea}} - \Delta\text{d}\delta_{\text{Condensation}}$. To simplify subscript labels, we use the same names for the last four components as the decomposition names of seasonal $\delta^{18}\text{O}_p$ variations, i.e., $\Delta\text{dP}_{\text{Ori}}$, $\Delta\text{d}\delta_{\text{Source}}$, $\Delta\text{d}\delta_{\text{Enroute}}$, and $\Delta\text{d}\delta_{\text{Condensation}}$. The interpretation of the anomaly is the difference between two time periods, similar to the case of seasonal cycle where the anomaly is the difference between two months. Finally, the annual $\delta^{18}\text{O}_p$ anomalies ($\Delta\delta^{18}\text{O}_{p,a}$) are ultimately decomposed into five components: $\Delta\text{dP}_{\text{Sea}}$, $\Delta\text{dP}_{\text{Ori}}$, $\Delta\text{d}\delta_{\text{Source}}$, $\Delta\text{d}\delta_{\text{Enroute}}$, and $\Delta\text{d}\delta_{\text{Condensation}}$ (Supplementary Fig. 14b).

For our purpose of analysis of EAM region here, we group the 25 source regions into six domains, the Pacific Ocean (PO), the Indian Ocean (IO), the Atlantic Ocean (AO), the local East Asia continent (EAS), the non-local Eurasian Continent (EC), and the remaining other source regions (Other). It should be noted that the EC includes Europe (EUR), Central Asia (CAS), and North Asia (NAS).

Data availability

The observed stable isotope data is available from the Global Network of Isotopes in Precipitation (GNIP) website (<https://nucleus.iaea.org/wiser>). The iCAM5.3 water tagging data is available on Zenodo⁸⁰ at <https://zenodo.org/records/15535268>.

Code availability

The iCESM is freely available as open-source code from <https://github.com/NCAR/iCESM1.2>. Data analysis and plotting were performed with NCL (NCAR Command Language, version 6.6.2, <https://www.ncl.ucar.edu/>). Main figure scripts are available from the corresponding authors upon request.

Received: 25 September 2024; Accepted: 5 June 2025;
Published online: 01 July 2025

References

- Dansgaard, W. Stable isotopes in precipitation. *Tellus* **16**, 436–468 (1964).
- Rozanski, K., Araguas-Araguas, L. & Gonfiantini, R. Isotopic patterns in modern global precipitation. *Clim. Change Cont. Isotopic Record* **78**, 1–36 (1993).
- Gat, J. R. Some classical concepts of isotope hydrology. in *Isotopes in the water cycle: past, present and future of a developing science* (Springer, 2005).
- Araguás-Araguás, L., Froehlich, K. & Rozanski, K. Stable isotope composition of precipitation over southeast Asia. *J. Geophys. Res. Atmos.* **103**, 28721–28742 (1998).
- Jouzel, J. et al. Orbital and millennial Antarctic climate variability over the past 800,000 years. *Science* **317**, 793–796 (2007).
- Tan, L. et al. Rainfall variations in central Indo-Pacific over the past 2,700 y. *Proc. Natl. Acad. Sci. USA* **116**, 17201–17206 (2019).
- Yang, B. et al. Long-term decrease in Asian monsoon rainfall and abrupt climate change events over the past 6,700 years. *Proc. Natl. Acad. Sci. USA* **118**, e2102007118 (2021).
- Zhao, L. et al. Factors controlling spatial and seasonal distributions of precipitation $\delta^{18}\text{O}$ in China. *Hydrol. Process.* **26**, 143–152 (2012).
- Wen, X. et al. Modeling precipitation $\delta^{18}\text{O}$ variability in East Asia since the last glacial maximum: temperature and amount effects across different timescales. *Clim. Past* **12**, 2077–2085 (2016).
- Wang, S. et al. Spatial and seasonal isotope variability in precipitation across China: monthly isoscapes based on regionalized fuzzy clustering. *J. Clim.* **35**, 3411–3425 (2022).
- Lee, J. E. et al. Asian monsoon hydrometeorology from TES and SCIAMACHY water vapor isotope measurements and LMDZ simulations: implications for speleothem climate record interpretation. *J. Geophys. Res. Atmos.* **117**, D15 (2012).
- Liu, Z. et al. Chinese cave records and the East Asia summer monsoon. *Quat. Sci. Rev.* **83**, 115–128 (2014).
- Cai, Z. & Tian, L. Atmospheric controls on seasonal and interannual variations in the precipitation isotope in the East Asian monsoon region. *J. Clim.* **29**, 1339–1352 (2016).
- Zhang, H. et al. East Asian hydroclimate modulated by the position of the westerlies during Termination I. *Science* **362**, 580–583 (2018).
- Hu, J., Emile-Geay, J., Tabor, C., Nusbaumer, J. & Partin, J. Deciphering oxygen isotope records from Chinese speleothems with an isotope-enabled climate model. *Paleoceanogr. Paleoclimat.* **34**, 2098–2112 (2019).
- Xu, C. et al. Tree-ring oxygen isotope across monsoon Asia: common signal and local influence. *Quat. Sci. Rev.* **269**, 107156 (2021).
- Chiang, J. et al. Enriched East Asian oxygen isotope of precipitation indicates reduced summer seasonality in regional climate and westerlies. *Proc. Natl. Acad. Sci. USA* **117**, 14745–14750 (2020).
- He, C. et al. Hydroclimate footprint of pan-Asian monsoon water isotope during the last deglaciation. *Sci. Adv.* **7**, eabe2611 (2021).
- Zhang, H. et al. The Asian summer monsoon: teleconnections and forcing mechanisms—A review from Chinese speleothem $\delta^{18}\text{O}$ records. *Quaternary* **2**, 26 (2019).
- Corrick, E. C. et al. Synchronous timing of abrupt climate changes during the last glacial period. *Science* **369**, 963–969 (2020).
- Battisti, D. S., Ding, Q. & Roe, G. H. Coherent pan-Asian climatic and isotopic response to orbital forcing of tropical insolation. *J. Geophys. Res. Atmos.* **119**, 11–997 (2014).
- Rao, Z., Li, Y., Zhang, J., Jia, G. & Chen, F. Investigating the long-term palaeoclimatic controls on the δD and $\delta^{18}\text{O}$ of precipitation during the Holocene in the Indian and East Asian monsoonal regions. *Earth Sci. Rev.* **159**, 292–305 (2016).
- Zhang, H. et al. A data-model comparison pinpoints Holocene spatiotemporal pattern of East Asian summer monsoon. *Quat. Sci. Rev.* **261**, 106911 (2021).
- Gourcy, L. L., Groening, M. & Aggarwal, P. K. Stable oxygen and hydrogen isotopes in precipitation. in *Isotopes in the water cycle: past, present and future of a developing science* (Springer, 2005).
- Tan, M. Circulation effect: response of precipitation $\delta^{18}\text{O}$ to the ENSO cycle in monsoon regions of China. *Clim. Dynam.* **42**, 1067–1077 (2014).
- Wu, H., Zhang, X., Xiaoyan, L., Li, G. & Huang, Y. Seasonal variations of deuterium and oxygen-18 isotopes and their response to moisture source for precipitation events in the subtropical monsoon region. *Hydrol. Process.* **29**, 90–102 (2015).
- Tang, Y. et al. Using stable isotopes to understand seasonal and interannual dynamics in moisture sources and atmospheric circulation in precipitation. *Hydrol. Process.* **31**, 4682–4692 (2017).
- Kong, Y., Wang, K., Li, J. & Pang, Z. Stable isotopes of precipitation in China: a consideration of moisture sources. *Water* **11**, 1239 (2019).
- Zhang, J. et al. Coupled effects of moisture transport pathway and convection on stable isotopes in precipitation across the East Asian monsoon region: Implications for paleoclimate reconstruction. *J. Clim.* **34**, 9811–9822 (2021).
- Xue, Y. et al. Quantifying source effects based on rainwater $\delta^{18}\text{O}$ from 10-year monitoring records in Southwest China. *Appl. Geochem.* **155**, 105706 (2023).
- Lin, F. et al. Seasonal to decadal variations of precipitation oxygen isotopes in northern China linked to the moisture source. *npj Clim. Atmos. Sci.* **7**, 14 (2024).
- Yuan, D. et al. Timing, duration, and transitions of the last interglacial Asian monsoon. *Science* **304**, 575–578 (2004).
- Ishizaki, Y. et al. Interannual variability of H_2^{18}O in precipitation over the Asian monsoon region. *J. Geophys. Res. Atmos.* **117**, D16308 (2012).
- Baker, A. J. et al. Seasonality of westerly moisture transport in the East Asian summer monsoon and its implications for interpreting precipitation $\delta^{18}\text{O}$. *J. Geophys. Res. Atmos.* **120**, 5850–5862 (2015).
- Orland, I. et al. Direct measurements of deglacial monsoon strength in a Chinese stalagmite. *Geology* **43**, 555–558 (2015).
- Yang, H., Johnson, K. R., Griffiths, M. L. & Yoshimura, K. Interannual controls on oxygen isotope variability in Asian monsoon precipitation and implications for paleoclimate reconstructions. *J. Geophys. Res. Atmos.* **121**, 8410–8428 (2016).
- Cai, Z., Tian, L. & Bowen, G. J. ENSO variability reflected in precipitation oxygen isotopes across the Asian Summer Monsoon region. *Earth Planet. Sci. Lett.* **475**, 25–33 (2017).
- Cai, Z., Tian, L. & Bowen, G. J. Spatial-seasonal patterns reveal large-scale atmospheric controls on Asian Monsoon precipitation water isotope ratios. *Earth Planet. Sci. Lett.* **503**, 158–169 (2018).
- Ruan, J., Zhang, H., Cai, Z., Yang, X. & Yin, J. Regional controls on daily to interannual variations of precipitation isotope ratios in Southeast China: implications for paleomonsoon reconstruction. *Earth Planet. Sci. Lett.* **527**, 115794 (2019).
- Zhou, H. et al. Variation of $\delta^{18}\text{O}$ in precipitation and its response to upstream atmospheric convection and rainout: a case study of Changsha station, south-central China. *Sci. Total Environ.* **659**, 1199–1208 (2019).
- Li, Y. et al. Variations of stable isotopic composition in atmospheric water vapor and their controlling factors—a 6-year continuous sampling study in Nanjing, eastern China. *J. Geophys. Res. Atmos.* **125**, e2019JD031697 (2020).
- Li, R. et al. Atmospheric process factors affecting the stable isotope variations in precipitation in Guiyang, Southwest China. *Theor. Appl. Climatol.* **155**, 3243–3257 (2024).
- Zhan, Z. et al. Determining key upstream convection and rainout zones affecting $\delta^{18}\text{O}$ in water vapor and precipitation based on 10-

- year continuous observations in the East Asian Monsoon region. *Earth Planet. Sci. Lett.* **601**, 117912 (2023).
44. Vuille, M., Werner, M., Bradley, R. S. & Keimig, F. Stable isotopes in precipitation in the Asian monsoon region. *J. Geophys. Res. Atmos.* **110**, D23 (2005).
 45. Wang, Y., Hu, C., Ruan, J. & Johnson, K. R. East Asian precipitation $\delta^{18}\text{O}$ relationship with various monsoon indices. *J. Geophys. Res. Atmos.* **125**, e2019JD032282 (2020).
 46. Wang, Y. et al. A high-resolution absolute-dated late Pleistocene monsoon record from Hulu Cave, China. *Science* **294**, 2345–2348 (2001).
 47. Cheng, H. et al. Ice age terminations. *Science* **326**, 248–252 (2009).
 48. Chiang, J. et al. Role of seasonal transitions and westerly jets in East Asian paleoclimate. *Quat. Sci. Rev.* **108**, 111–129 (2015).
 49. Zhang, H. et al. A 200-year annually laminated stalagmite record of precipitation seasonality in southeastern China and its linkages to ENSO and PDO. *Sci. Rep.* **8**, 12344 (2018).
 50. Zhang, H. et al. Effect of precipitation seasonality on annual oxygen isotopic composition in the area of spring persistent rain in southeastern China and its paleoclimatic implication. *Clim. Past* **16**, 211–225 (2020).
 51. Shi, Y., Jiang, Z., Liu, Z. & Li, L. A Lagrangian analysis of water vapor sources and pathways for precipitation in East China in different stages of the East Asian summer monsoon. *J. Clim.* **33**, 977–992 (2020).
 52. Sodemann, H., Schwierz, C. & Wernli, H. Interannual variability of Greenland winter precipitation sources: Lagrangian moisture diagnostic and North Atlantic Oscillation influence. *J. Geophys. Res. Atmos.* **113**, D3 (2008).
 53. Pausata, S. F. R., Battisti, D. S., Kerim, H., Nisancioglu, K. H. & Bitz, C. M. Chinese stalagmite $\delta^{18}\text{O}$ controlled by changes in the Indian monsoon during a simulated Heinrich event. *Nat. Geosci.* **4**, 474–480 (2011).
 54. Singh, H. A., Bitz, C. M., Nusbaumer, J. & Noone, D. C. A mathematical framework for analysis of water tracers: Part 1: development of theory and application to the preindustrial mean state. *J. Adv. Model. Earth Sys.* **8**, 991–1013 (2016).
 55. Werner, M., Mikolajewicz, U., Heimann, M. & Hoffmann, G. Borehole versus isotope temperatures on Greenland: seasonality does matter. *Geophys. Res. Lett.* **27**, 723–726 (2000).
 56. He, C. et al. Abrupt Heinrich Stadial 1 cooling missing in Greenland oxygen isotopes. *Sci. Adv.* **7**, eabh1007 (2021).
 57. Tabor, C. R. et al. Interpreting precession-driven $\delta^{18}\text{O}$ variability in the South Asian monsoon region. *J. Geophys. Res. Atmos.* **123**, 5927–5946 (2018).
 58. Wen, Q. et al. Grand dipole response of Asian summer monsoon to orbital forcing. *npj Clim. Atmos. Sci.* **7**, 202 (2024).
 59. Risi, C. et al. Understanding the Sahelian water budget through the isotopic composition of water vapor and precipitation. *J. Geophys. Res. Atmos.* **115**, 1–23 (2010).
 60. Cheng, H. et al. Milankovitch theory and monsoon. *Innovation* **3**, 100338 (2022).
 61. Tan, L., Cai, Y., Cheng, H., An, Z. & Edwards, R. L. Summer monsoon precipitation variations in central China over the past 750 years derived from a high-resolution absolute-dated stalagmite. *Palaeogeogr. Palaeoclimatol. Palaeoecol.* **280**, 432–439 (2009).
 62. Tan, L. et al. Climate significance of speleothem $\delta^{18}\text{O}$ from central China on decadal timescale. *J. Asian Earth Sci.* **106**, 150–155 (2015).
 63. Tan, L. et al. Centennial-to decadal-scale monsoon precipitation variations in the upper Hanjiang River region, China over the past 6650 years. *Earth Planet. Sci. Lett.* **482**, 580–590 (2018).
 64. Lu, J. et al. A 120-year seasonally resolved speleothem record of precipitation seasonality from southeastern China. *Quat. Sci. Rev.* **264**, 107023 (2021).
 65. Shi, F., et al. Interdecadal to multidecadal variability of East Asian summer monsoon over the past half millennium. *J. Geophys. Res. Atmos.* **127**, e2022JD037260 (2022).
 66. Brady, E. et al. The connected isotopic water cycle in the community Earth system model version 1. *J. Adv. Model. Earth Sys.* **11**, 2547–2566 (2019).
 67. McManus, J. F., Oppo, D. W. & Cullen, J. L. A 0.5-million-year record of millennial-scale climate variability in the North Atlantic. *Science* **283**, 971–975 (1999).
 68. Lynch-Stieglitz, J. The Atlantic meridional overturning circulation and abrupt climate change. *Annu. Rev. Mar. Sci.* **9**, 83–104 (2017).
 69. Cheng, H. et al. The Asian monsoon over the past 640,000 years and ice age terminations. *Nature* **534**, 640–646 (2016).
 70. Sun, Y. et al. Persistent orbital influence on millennial climate variability through the Pleistocene. *Nat. Geosci.* **14**, 812–818 (2021).
 71. Wiersma, A. P. & Renssen, H. Model–data comparison for the 8.2 ka BP event: confirmation of a forcing mechanism by catastrophic drainage of Laurentide Lakes. *Quat. Sci. Rev.* **25**, 63–88 (2006).
 72. Matero, I. S. O., Gregoire, L. J., Ivanovic, R. F., Tindall, J. C. & Haywood, A. M. The 8.2 ka cooling event caused by Laurentide ice saddle collapse. *Earth Planet. Sci. Lett.* **473**, 205–214 (2017).
 73. Wu, C. H. & Tsai, P. C. Obliquity-driven changes in East Asian seasonality. *Glob. Planet. Change* **189**, 103161 (2020).
 74. Yan, M. et al. Relationship between the East Asian summer and winter monsoons at obliquity time scales. *J. Clim.* **36**, 3993–4003 (2023).
 75. Cheng, H. et al. A penultimate glacial monsoon record from Hulu Cave and two-phase glacial terminations. *Geology* **34**, 217–220 (2006).
 76. Wang, Y. et al. Millennial-and orbital-scale changes in the East Asian monsoon over the past 224,000 years. *Nature* **451**, 1090–1093 (2008).
 77. Li, H. C. et al. The $\delta^{18}\text{O}$ and $\delta^{13}\text{C}$ records in an aragonite stalagmite from Furong Cave, Chongqing, China: A-2000-year record of monsoonal climate. *J. Asian Earth Sci.* **40**, 1121–1130 (2011).
 78. Atwood, A. R., Battisti, D. S., Wu, E., Frierson, D. M. W. & Sachs, J. P. Data-model comparisons of tropical hydroclimate changes over the common era. *Paleoceanogr. Paleoclimatol.* **36**, e2020PA003934 (2021).
 79. Bühler, J. C. et al. Investigating stable oxygen and carbon isotopic variability in speleothem records over the last millennium using multiple isotope-enabled climate models. *Clim. Past* **18**, 1625–1654 (2022).
 80. Jing, Z., Liu, Z., He, C. & Wen, Q. iCAM5.3 water tagging dataset cross seasonal, millennial, and precessional timescales. Zenodo. <https://doi.org/10.5281/zenodo.15535268> (2025).

Acknowledgements

This work was jointly funded by the National Natural Science Foundation of China (42301023, 42361164616, 32301501), the Science and Technology Innovation Project of Laoshan Laboratory (LSKJ202203303, LSKJ202302400-03, LSKJ202202200-04), Shandong Province's "Taishan" Scientist Program (grant no. ts201712017), and IAP Innovation Computing Project (2024-EL-ZD-000170).

Author contributions

Conceptualization: Z.L. and Z.J. Methodology: Z.L., Z.J., Q.W., and C.H. Visualization: Z.J. Supervision: Z.L. and S.Z. Writing—original draft: Z.J., Z.L., S.Z., Q.W., C.H., Y.B., and W.Y.

Competing interests

The authors declare no competing interests.

Additional information

Supplementary information The online version contains supplementary material available at <https://doi.org/10.1038/s43247-025-02448-1>.

Correspondence and requests for materials should be addressed to Zhengyu Liu or Shaoqing Zhang.

Peer review information *Communications Earth & Environment* thanks Qiong Zhang and the other, anonymous, reviewer(s) for their contribution to the peer review of this work. Primary Handling Editors: Yiming Wang and Carolina Ortiz Guerrero. [A peer review file is available].

Reprints and permissions information is available at <http://www.nature.com/reprints>

Publisher's note Springer Nature remains neutral with regard to jurisdictional claims in published maps and institutional affiliations.

Open Access This article is licensed under a Creative Commons Attribution-NonCommercial-NoDerivatives 4.0 International License, which permits any non-commercial use, sharing, distribution and reproduction in any medium or format, as long as you give appropriate credit to the original author(s) and the source, provide a link to the Creative Commons licence, and indicate if you modified the licensed material. You do not have permission under this licence to share adapted material derived from this article or parts of it. The images or other third party material in this article are included in the article's Creative Commons licence, unless indicated otherwise in a credit line to the material. If material is not included in the article's Creative Commons licence and your intended use is not permitted by statutory regulation or exceeds the permitted use, you will need to obtain permission directly from the copyright holder. To view a copy of this licence, visit <http://creativecommons.org/licenses/by-nc-nd/4.0/>.

© The Author(s) 2025